

Photoinduced topological phase transition in monolayer 1T'-MoS₂

Mohammad Mortezaei Nobahari  *

Department of Physics, Ferdowsi University of Mashhad, Iran

(Dated: November 20, 2025)

We investigate the nonequilibrium topological phases of monolayer 1T'-MoS₂ under high-frequency circularly polarized driving using a low-energy $k \cdot p$ Hamiltonian combined with a van Vleck expansion. The off-resonant field generates spin- and valley-dependent mass corrections that reshape the Berry curvature profile and shift the conditions for band inversion. By evaluating the quasienergy bands, Berry curvatures, Hall conductivities, and spin- valley-resolved Chern numbers, we identify a sequence of light-controlled topological transitions marked by well-defined gap closings. Depending on the Floquet coupling strength and the electric-field parameter, the system evolves between the equilibrium quantum spin Hall (QSH) state and a set of driven phases including spin-polarized quantum Hall insulator (S-QHI), quantum valley Hall (QVH or BI) and photo-induced quantum Hall insulator (P-QHI) regimes. The results establish 1T'-MoS₂ as a tunable platform where circular driving selectively manipulates spin and valley degrees of freedom, enabling controlled access to non-equilibrium topological phases in transition-metal dichalcogenides.

I. INTRODUCTION

The discovery of topological phases of matter has profoundly reshaped modern condensed matter physics, uncovering quantum states that are characterized not merely by broken symmetries but by global topological invariants defined in momentum space. Among these, the quantum spin Hall (QSH) effect stands as a cornerstone of two-dimensional (2D) topological physics, representing a time-reversal-symmetric analogue of the quantum Hall effect, where counterpropagating spin-polarized edge states coexist at opposite boundaries of an insulating bulk [1–4]. These helical edge modes are protected by time-reversal symmetry (\mathcal{T}) and are immune to non-magnetic backscattering, leading to dissipationless spin currents and quantized edge conductance of $2e^2/h$ [5–7].

Theoretical proposals of the QSH effect in graphene [1] demonstrated the essential role of spin-orbit coupling (SOC) in generating a nontrivial topological gap, though the small SOC in graphene limited experimental realization. This challenge was overcome by Bernevig, Hughes, and Zhang in HgTe/CdTe quantum wells, where a thickness-tuned band inversion produced a measurable QSH phase [8]. The experimental observation of the QSH effect in these wells [9] inaugurated the era of 2D topological insulators (TIs), motivating extensive efforts to identify new material platforms with large band gaps, chemical stability, and compatibility with devices [10, 11].

In the ensuing decade, the QSH state has been realized or proposed in a wide variety of 2D systems, including InAs/GaSb quantum wells [12, 13], silicene and germanene [14, 15], bismuth bilayers [16, 17], stanene [18], and particularly transition-metal dichalcogenides (TMDs) in their distorted 1T' phase [19–21]. The topological character of these materials is typically characterized through the \mathbb{Z}_2 invariant or the spin Chern number [22], both of which relate to the Berry curvature distribution and band inversion near the Fermi level.

The bulk–edge correspondence implies that a nontriv-

ial topological invariant guarantees the presence of gapless helical edge states traversing the bulk gap [6, 7]. These edge modes yield quantized spin Hall conductance and are robust against time-reversal-preserving perturbations, contrasting with the quantum anomalous Hall effect (QAHE), where \mathcal{T} symmetry is broken by magnetism [23–25]. The interplay between SOC, crystal symmetry, and inversion-breaking perturbations determines the onset of QSH behavior, and recent work has emphasized the tunability of these properties via strain, electric fields, or light–matter coupling [26–29].

In parallel, the discovery of atomically thin van der Waals materials has provided an ideal playground for realizing 2D topological phases. Among them, transition-metal dichalcogenides (TMDs) with formula MX₂ (M = Mo, W; X = S, Se, Te) have attracted enormous attention due to their rich polymorphism and strong SOC [30–32]. The semiconducting 2H phase of MoS₂ is the most widely studied, exhibiting a direct band gap of about 1.8 eV in the monolayer limit and valley-selective circular dichroism [33, 34]. However, metastable metallic 1T and semimetallic 1T' phases of MoS₂ exhibit drastically different properties, including Peierls distortions, charge density wave instabilities, and topologically non-trivial band orderings [35].

The distorted 1T' phase, characterized by a zigzag chain of Mo atoms, has been theoretically predicted to host a robust QSH state with an energy gap on the order of 0.1–0.3 eV, suitable for room-temperature operation [19]. First-principles calculations revealed that strong SOC and lattice distortion drive band inversion between Mo- d and S- p orbitals near the Γ point, resulting in a nontrivial \mathbb{Z}_2 topology [19, 36]. Experimental signatures of this topological insulating phase have been reported in monolayer WTe₂ [21, 37], and related observations in Mo-based TMDs suggest a shared underlying mechanism [38, 39]. In 1T'-MoS₂, the magnitude of the SOC and the presence of inversion asymmetry further enrich its spin and valley physics, making it a compelling platform for exploring QSH and valley Hall effects [40].

The ability to manipulate the topological character of 1T'-MoS₂ using external fields or optical driving opens exciting prospects for nonequilibrium topological phenomena. Floquet engineering—the periodic modulation of a system by light—has emerged as a powerful tool to dynamically induce and tune topological states [41, 42]. When a 1T'-MoS₂ monolayer is subjected to a circularly polarized field, the effective Hamiltonian acquires light-induced mass terms that modify the Berry curvature and band topology, leading to Floquet–Bloch bands with controllable Chern numbers [43–45]. Such light-driven transitions between trivial, QSH, and quantum anomalous Hall phases have been theoretically demonstrated in several 2D materials [46–48], making 1T'-MoS₂ an ideal candidate for tunable topological spintronics.

Time-periodic driving is a versatile tool to create and control topological phases that do not exist in equilibrium. A canonical example is the generation of Haldane-like masses in Dirac materials by circularly polarized light (CPL), which breaks time-reversal symmetry and can convert a quantum spin Hall state into a quantum anomalous Hall state. Monolayer 1T'-MoS₂ exhibits strong spin–orbit coupling and a low-energy bandstructure amenable to an effective two-band description; this makes it an excellent platform for Floquet-driven topological transitions. Our results demonstrate that suitable tuning of the external fields enables the system to transition among the QSH, QVH (or BI), P-QHI, and S-QHI phases.

In this paper, we focus on the spin- and valley-resolved Hall conductivity of monolayer 1T'-MoS₂ under periodic driving. By introducing a tunable Floquet parameter ξ , we demonstrate how light–matter coupling can modify the band inversion, Berry curvature distribution, and Hall conductivity, revealing a controllable crossover between topological and trivial regimes. The obtained results provide theoretical guidance for future experimental efforts toward optically tunable topological devices based on 1T'-phase TMDs.

II. THEORY

Figures 1(a) and 1(b) depict the side and top views of monolayer 1T'-MoS₂, respectively. This two-dimensional material comprises two atomic species: molybdenum (Mo), shown in green, and sulfur (S), shown in dark-gray. The primitive unit cell, highlighted by a green parallelogram, contains four atoms.

The low-energy $\mathbf{k} \cdot \mathbf{p}$ Hamiltonian of monolayer 1T'-MoS₂ in the x - y plane, subject to a perpendicular electric field E_z and gate voltage V , has been previously established in Refs. [19, 49, 50]. The total Hamiltonian is expressed as the sum of the intrinsic Hamiltonian $H_{k,p}$, the electric field contribution H_{E_z} , and the gate potential V :

$$H = H_{k,p} + H_{E_z} + V. \quad (1)$$

The unperturbed Hamiltonian $H_{k,p}$ is given by:

$$H_{k,p} = \begin{pmatrix} E_p & 0 & -i\hbar\nu_1 q_y & \hbar\nu_2 q_y \\ 0 & E_p & \hbar\nu_2 q_y & -i\hbar\nu_1 q_x \\ i\hbar\nu_1 q_x & \hbar\nu_2 q_y & E_d & 0 \\ \hbar\nu_2 q_y & i\hbar\nu_1 q_x & 0 & E_d \end{pmatrix}, \quad (2)$$

and the contribution from the electric field is:

$$H_{E_z} = \alpha \Delta_{\text{SO}} \begin{pmatrix} 0 & 0 & 1 & 0 \\ 0 & 0 & 0 & 1 \\ 1 & 0 & 0 & 0 \\ 0 & 1 & 0 & 0 \end{pmatrix}, \quad (3)$$

where V is a diagonal 4×4 matrix, and $\Delta_{\text{SO}} = 41.9$ meV denotes the intrinsic SOC gap at the Dirac points $(0, \kappa\Lambda)$. The dimensionless parameter $\alpha = |E_z/E_c|$, with $E_c = 1.42$ V/nm being the critical electric field required to induce a topological phase transition.

The on-site energies for the p - and d -orbitals are defined as:

$$E_p = \delta_p + \frac{\hbar^2 q_x^2}{2m_x^p} + \frac{\hbar^2 q_y^2}{2m_y^p}, \quad (4)$$

$$E_d = \delta_d + \frac{\hbar^2 q_x^2}{2m_x^d} + \frac{\hbar^2 q_y^2}{2m_y^d}, \quad (5)$$

where $\delta_p = 0.46$ eV, $\delta_d = -0.20$ eV, $m_x^p = -0.50m_0$, $m_y^p = -0.16m_0$, $m_x^d = 2.48m_0$, $m_y^d = 0.37m_0$, and m_0 is the free electron mass. The Fermi velocities along the x - and y -directions are $\nu_1 = 3.87 \times 10^5$ m/s and $\nu_2 = 0.46 \times 10^5$ m/s, respectively.

After applying a unitary transformation, the effective Hamiltonian in the spin and valley basis becomes:

$$H_{\kappa,s}(k) = \hbar k_x \nu_1 \sigma_y - \hbar k_y (s \nu_2 \sigma_x + \kappa \nu_- \sigma_0 + \kappa \nu_+ \sigma_z) + \Delta_{\text{so}}(\alpha - s\kappa) \sigma_x + V \sigma_0 \quad (6)$$

where $s = \pm 1$ denotes spin-up and spin-down states, and $\kappa = \pm 1$ labels the K and K' valleys, respectively. The tilting velocities ν_{\pm} are given by:

$$\nu_- = \frac{\hbar q_0}{2} \left(-\frac{1}{m_y^p} - \frac{1}{m_y^d} \right) = 2.84 \times 10^5 \text{ m/s}, \quad (7)$$

$$\nu_+ = \frac{\hbar q_0}{2} \left(-\frac{1}{m_y^p} + \frac{1}{m_y^d} \right) = 7.18 \times 10^5 \text{ m/s}. \quad (8)$$

This effective Hamiltonian captures the anisotropic band structure and tunable topological properties of the 1T'-MoS₂ monolayer under external electric field.

It is convenient to write Hamiltonian as $H = d(k) \cdot \sigma + d_0 \sigma_0$. After diagonalization of the Hamiltonian we have

$$\varepsilon_{\kappa,s}^{\pm}(k_x, k_y) = d_0(k_y) \pm \sqrt{[d_x(k_y)]^2 + [d_y(k_x)]^2 + [d_z(k_y)]^2} \quad (9)$$

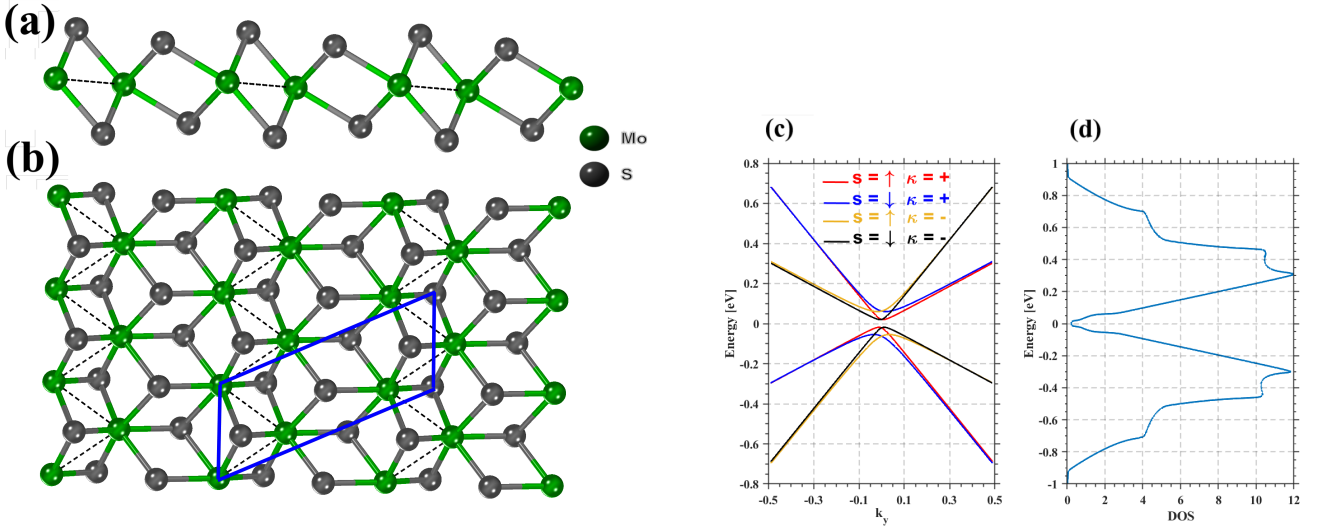


FIG. 1: (a) Side view and (b) top view of the crystal structure of monolayer 1T'-MoS₂. Molybdenum (Mo) and sulfur (S) atoms are represented by green and dark-gray spheres, respectively. The dashed lines highlight the Mo-Mo dimerization pattern, and the blue parallelogram marks the primitive unit cell used in our calculations. (c) Spin- and valley-resolved band structure of monolayer 1T'-MoS₂ near the Fermi level, showing the effects of SOC and valley asymmetry. The red and blue curves correspond to the spin-up and spin-down states at the $\kappa = +$ valley, while the yellow and black curves represent the same at the $\kappa = -$ valley. A small gap opening at $k_y = 0$ reflects SOC-induced band splitting. (d) Corresponding DOS illustrating a small minimum near the Fermi energy and pronounced van Hove singularities on both sides, consistent with the anisotropic band structure of the 1T' phase.

and corresponding eigenstates are

$$\psi_{\kappa,s}^{\pm}(k_x, k_y) = \left(\frac{\mp i d_y(k_x) \mp d_x(k_y)}{\pm d_z(k_y) + \sqrt{[d_x(k_y)]^2 + [d_y(k_x)]^2 + [d_z(k_y)]^2}} \right) \quad (10)$$

where

$$d_x^0(k_y) = \Delta_{so}(\alpha - s\kappa) - \hbar k_y s \nu_2 \quad (11)$$

$$d_y^0(k_x) = \hbar k_x \nu_1 \quad (12)$$

$$d_z^0(k_y) = \hbar k_y \kappa \nu_+ \quad (13)$$

$$d_0(k_y) = V - \hbar k_y \kappa \nu_- \quad (14)$$

and the mass vectors are

$$M_x^0 = d_x^0(0) = \Delta_{so}(\alpha - s\kappa) \quad (15)$$

$$M_y^0 = d_y^0(0) = 0 \quad (16)$$

$$M_z^0 = d_z^0(0) = 0 \quad (17)$$

A. Coupling to a periodic drive

We consider spatially-uniform circularly polarized light in the dipole approximation. The vector potential is

$$\mathbf{A}(t) = A_0 (\cos(\omega t), \eta \sin(\omega t)), \quad (18)$$

$$\eta = \pm 1 \text{ (right/left helicity),}$$

and minimal coupling is implemented via $\mathbf{k} \mapsto \mathbf{k} + \frac{e}{\hbar} \mathbf{A}(t)$.

Retaining terms linear in \mathbf{A} (the paramagnetic coupling; the A^2 diamagnetic scalar contributes only an overall Stark shift to leading order) the time-dependent Hamiltonian becomes

$$H_{\kappa s}(t) = H_{\kappa s}(k) + e \nu_1 A_x(t) \sigma_y - e A_y(t) \Pi_{\kappa s}, \quad (19)$$

where we defined

$$\Pi_{\kappa s} \equiv s \nu_2 \sigma_x + \kappa \nu_- \sigma_0 + \kappa \nu_+ \sigma_z. \quad (20)$$

For a $T = 2\pi/\omega$ -periodic Hamiltonian the Schrödinger equation admits Floquet solutions $\Psi_{\alpha}(t) = e^{-i\epsilon_{\alpha}t/\hbar} \Phi_{\alpha}(t)$ with $\Phi_{\alpha}(t+T) = \Phi_{\alpha}(t)$. In the off-resonant (high-frequency) regime, $\hbar\omega$ is taken larger than the bandwidth and relevant interband energies, avoiding real photon absorption; then a controlled expansion (van Vleck / Floquet-Magnus) yields an effective static Floquet Hamiltonian

$$H_F = H^{(0)} + \frac{1}{\hbar\omega} [H_{-1}, H_{+1}] + \mathcal{O}(\omega^{-2}), \quad (21)$$

$$H_{(\pm 1)} \equiv \frac{1}{T} \int_0^T dt H(t) e^{\pm i\omega t}, \quad (22)$$

where $H_{\pm 1}$ are the $\pm\omega$ Fourier components of $H(t)$.
Using

$$A_x(t) = \frac{A_0}{2} (e^{i\omega t} + e^{-i\omega t}), \quad A_y(t) = \frac{\eta A_0}{2i} (e^{i\omega t} - e^{-i\omega t}),$$

the Fourier components from Eq. (22) are

$$H_{+1} = \frac{eA_0}{2} \left(\nu_1 \sigma_y + \frac{\eta}{i} \Pi_{\kappa s} \right), \quad (23)$$

$$H_{-1} = \frac{eA_0}{2} \left(\nu_1 \sigma_y - \frac{\eta}{i} \Pi_{\kappa s} \right). \quad (24)$$

A direct commutator evaluation (using $[\sigma_y, \sigma_x] = -2i\sigma_z$ and $[\sigma_y, \sigma_z] = 2i\sigma_x$) gives

$$[H_{-1}, H_{+1}] = e^2 \nu_1 \eta A_0^2 (\kappa \nu_+ \sigma_x - s \nu_2 \sigma_z). \quad (25)$$

Substituting Eq. (25) into Eq. (21) yields the effective Floquet Hamiltonian to leading order in $1/\omega$:

$$\delta H_F^{(\kappa s)} = \frac{e^2 \nu_1 A_0^2}{\hbar \omega} \eta (\kappa \nu_+ \sigma_x - s \nu_2 \sigma_z). \quad (26)$$

and total Hamiltonian is

$$\begin{aligned} H_F^{(\kappa s)}(\mathbf{k}) &\approx \hbar k_x \nu_1 \sigma_y - \hbar k_y (s \nu_2 \sigma_x + \kappa \nu_- \sigma_0 - \kappa \nu_+ \sigma_z) \\ &+ \left[\Delta_{\text{so}}(\alpha - s\kappa) + \xi \nu_+ \eta \kappa \right] \sigma_x \\ &- \xi \nu_2 \eta s \sigma_z + V \sigma_0. \end{aligned} \quad (27)$$

where we defined $\xi \equiv \frac{e^2 \nu_1}{\hbar \omega} A_0^2$

B. Mass vector, spectrum and light-shifted criticality

It is convenient to write $H_F = \mathbf{d}'(\mathbf{k}) \cdot \boldsymbol{\sigma} + d_0(\mathbf{k}) \sigma_0$ with components

$$d'_x(\mathbf{k}) = -\hbar k_y s \nu_2 + \Delta_{\text{so}}(\alpha - s\kappa) + \xi \nu_+ \eta \kappa, \quad (28)$$

$$d'_y(\mathbf{k}) = \hbar k_x \nu_1, \quad (29)$$

$$d'_z(\mathbf{k}) = -\hbar k_y \kappa \nu_+ - \xi \nu_2 \eta s, \quad (30)$$

$$d_0(\mathbf{k}) = V - \hbar k_y \kappa \nu_-. \quad (31)$$

The quasienergies are $\epsilon^\pm(\mathbf{k}) = d_0(\mathbf{k}) \pm \sqrt{d_x'^2 + d_y'^2 + d_z'^2}$.

At $\mathbf{k} = 0$ the drive produces two Floquet shifted effective masses contributions

$$M_x \equiv d'_x(0) = \Delta_{\text{so}}(\alpha - s\kappa) + \xi \nu_+ \eta \kappa, \quad (32)$$

$$M_y \equiv d'_y(0) = 0 \quad (33)$$

$$M_z \equiv d'_z(0) = -\xi \nu_2 \eta s. \quad (34)$$

Therefore the quasieigenvalues at $\mathbf{k} = 0$ are $\epsilon^\pm(0) = V \pm \sqrt{M_x^2 + M_z^2}$.

The CPL-induced shift of the σ_x mass moves the critical band-inversion parameter to

$$\alpha_c^{(\kappa s)} = s\kappa - \frac{\xi \nu_+}{\Delta_{\text{so}}} \kappa \eta. \quad (35)$$

Simultaneously, M_z acts as a spin-selective mass (it is proportional to s), which can prevent an exact gap closure at $\mathbf{k} = 0$ unless compensated by finite k_y or by tuning parameters.

C. Berry Curvature of the Floquet Hamiltonian

For a generic two-band Hamiltonian of the form

$$H(\mathbf{k}) = d_0(\mathbf{k}) \sigma_0 + \mathbf{d}'(\mathbf{k}) \cdot \boldsymbol{\sigma}, \quad (36)$$

with $\mathbf{d}'(\mathbf{k}) = (d'_x, d'_y, d'_z)$, the Berry curvature of the upper (+) and lower (−) bands is given by

$$\Omega_\pm^z(\mathbf{k}) = \pm \frac{1}{2} \frac{\mathbf{d}' \cdot (\partial_{k_x} \mathbf{d}' \times \partial_{k_y} \mathbf{d}')}{|\mathbf{d}'|^3}, \quad |\mathbf{d}'| = \sqrt{d_x'^2 + d_y'^2 + d_z'^2}. \quad (37)$$

The scalar term $d_0(\mathbf{k})$ only shifts the energy and does not contribute.

For the Floquet effective Hamiltonian of monolayer 1T'-MoS₂ under circularly polarized light we obtained

$$d'_x = -\hbar k_y s \nu_2 + M_x, \quad (38)$$

$$d'_y = \hbar k_x \nu_1, \quad (39)$$

$$d'_z = -\hbar k_y \kappa \nu_+ + M_z, \quad (40)$$

$$d_0 = V - \hbar k_y \kappa \nu_-, \quad (41)$$

Evaluating the derivatives,

$$\partial_{k_x} \mathbf{d}' = (0, \hbar \nu_1, 0), \quad \partial_{k_y} \mathbf{d}' = (-\hbar s \nu_2, 0, -\hbar \kappa \nu_+), \quad (42)$$

one finds

$$\mathbf{d}' \cdot (\partial_{k_x} \mathbf{d}' \times \partial_{k_y} \mathbf{d}') = \hbar^2 \nu_1 (\kappa \nu_+ M_x - s \nu_2 M_z), \quad (43)$$

which is independent of \mathbf{k} .

The final Berry curvature of the lower band is therefore

$$\Omega_+^z(\mathbf{k}) = \frac{\hbar^2 \nu_1}{2} \frac{\kappa \nu_+ M_x - s \nu_2 M_z}{|\mathbf{d}'|^3} \quad (44)$$

where

$$|\mathbf{d}'|^3 = [(M_x - \hbar k_y s \nu_2)^2 + (\hbar k_x \nu_1)^2 + (M_z - \hbar k_y \kappa \nu_+)^2]^{3/2} \quad (45)$$

while the lower band has the opposite sign,

$$\Omega_-^z(\mathbf{k}) = -\Omega_+^z(\mathbf{k}). \quad (46)$$

Note that the tilt velocity ν_- and scalar potential V appear only in d_0 and therefore do not affect the Berry curvature. The sign and magnitude of the curvature are controlled by the effective Floquet masses M_x and M_z , which depend explicitly on the light helicity η and amplitude A_0 .

D. Hall conductivity

We begin from the Berry curvature of the upper Floquet band for a given valley $\kappa = \pm 1$ and spin $s = \pm 1$,

$$\Omega_+^z(\mathbf{k}) = \frac{\hbar^2 \nu_1}{2} \frac{B M_x - A M_z}{|d'|^3}, \quad (47)$$

where, for compactness, we defined

$$A \equiv s \nu_2, \quad B \equiv \kappa \nu_+,$$

The zero-temperature intrinsic Hall conductivity (chemical potential inside the gap) for sector (κ, s) is

$$\sigma_{xy}^{(\kappa s)} = \frac{e^2}{\hbar} \int_{\mathbb{R}^2} \frac{d^2 k}{(2\pi)} \Omega^z(\mathbf{k}) = \frac{e^2}{\hbar} C_{\kappa s}, \quad (48)$$

with the Chern number

$$C_{\kappa s} = \frac{1}{2\pi} \int_{\mathbb{R}^2} d^2 k \Omega^z(\mathbf{k}). \quad (49)$$

The Chern number formula can be written as (see Appendix V)

$$C_{\kappa s} = \frac{1}{2} \text{sgn}(\kappa \nu_+ M_x - s \nu_2 M_z). \quad (50)$$

Let $C_{\kappa s}$ denote the Chern number of the occupied band manifold in valley $\kappa = \pm$ and spin channel $s = \uparrow, \downarrow$. The total Chern number is then

$$C_{\text{tot}}(\xi) = \sum_{\kappa=\pm} \sum_{s=\uparrow, \downarrow} C_{\kappa s} = \sum_s C_s(\xi) = \sum_{\kappa} C_{\kappa}(\xi), \quad (51)$$

where $C_s(\xi) = \sum_{\kappa} C_{\kappa s}$ and $C_{\kappa}(\xi) = \sum_s C_{\kappa s}$ are the spin- and valley-resolved Chern numbers, respectively. We further define

$$\Delta C_{\text{valley}} = \frac{C_+ - C_-}{2}, \quad \Delta C_{\text{spin}} = \frac{C_{\uparrow} - C_{\downarrow}}{2}. \quad (52)$$

III. RESULTS AND DISCUSSION

Figures 1(c) and 1(d) display the low-energy band dispersion and the corresponding density of states (DOS) for monolayer 1T'-MoS₂ near the Fermi level, revealing the essential electronic features that underpin its topological behavior. In Fig. 1(c), the band structure is resolved according to spin ($S = \uparrow, \downarrow$) and valley ($\kappa = \pm$) indices,

highlighting the spin-valley coupling inherent to the 1T' phase. The red and blue curves correspond to spin-up and spin-down states at the $\kappa = +$ valley, respectively, whereas the yellow and black curves represent the spin-up and spin-down branches at the $\kappa = -$ valley.

At $k_y = 0$, a small band gap opens at the crossing point, evidencing the presence of SOC, which lifts the degeneracy and separates the spin-resolved branches. The asymmetry between the spin-up and spin-down dispersions reflects the broken inversion symmetry of the system combined with strong SOC originating from the Mo d orbitals. The linear crossing of the conduction and valence bands near the Fermi level indicates Dirac-like behavior modified by SOC, which transforms the massless Dirac fermions into massive ones and results in a topological insulating phase depending on the sign of the band inversion parameter.

Figure 1(d) presents the corresponding DOS, which is consistent with the features observed in the band structure. Near the Fermi energy ($E = 0$), the DOS exhibits a minimum corresponding to the small band gap. The sharp peaks on both sides of the Fermi level arise from van Hove singularities associated with the nearly flat portions of the bands at higher energies.

Figure 2 (a-f) summarizes the Floquet quasienergy dispersions and the corresponding Berry curvature distributions of monolayer 1T'-MoS₂ for representative values of the light-matter coupling ξ , the electric field α , and valley index κ for different spin configurations. The magnitude of the Berry curvatures are renormalized to fit in the figures. In panel 2(a) ($\alpha < 1$, $\xi = 0.02$, $\kappa = -1$) the conduction and valence bands meet at $k_y = 0$ with an essentially linear crossing; no direct gap is resolved at the valley center in the plotted window. The Berry curvature in this panel is sharply localized around the crossing point and vanishes slightly away from that. Panel 2(b) shows a modest Floquet-induced hybridization at $k_y \approx 0$, i.e., a small but finite avoided crossing; the Berry curvature remains same-signed and comparable across the two spin branches. Panels 2(c) and 2(d) correspond to stronger driving ($\xi = 0.064$) for $\alpha < 1$ and $\alpha > 1$, respectively, with strong band curvature near the gap edges. In these strong-coupling panels the Berry curvature is sharply localized at the gap flanks, attains the largest amplitudes of the series, and shows the same sign for spin-up and spin-down channels; the two valleys display the expected valley-dependent inversion of band slopes while preserving the same qualitative curvature enhancement under increased ξ . Finally, panels 2 (e) and (f) (strong coupling) there is a large gap opening in comparison with other panels (see panel (e)). In this case the Berry curvatures reduced and for both spin configurations remain same-signed around the $k_y = 0$, and for $\alpha > 1$ and $\kappa = -1$ (panel 2 (f)) there is a band crossing and the Berry curvature is sharply localized at $k_y = 0$.

Figure 3 (a - d) presents the anomalous spin-valley-resolved Hall conductivity versus Fermi energy for different Floquet coupling strengths ξ . In the absence of

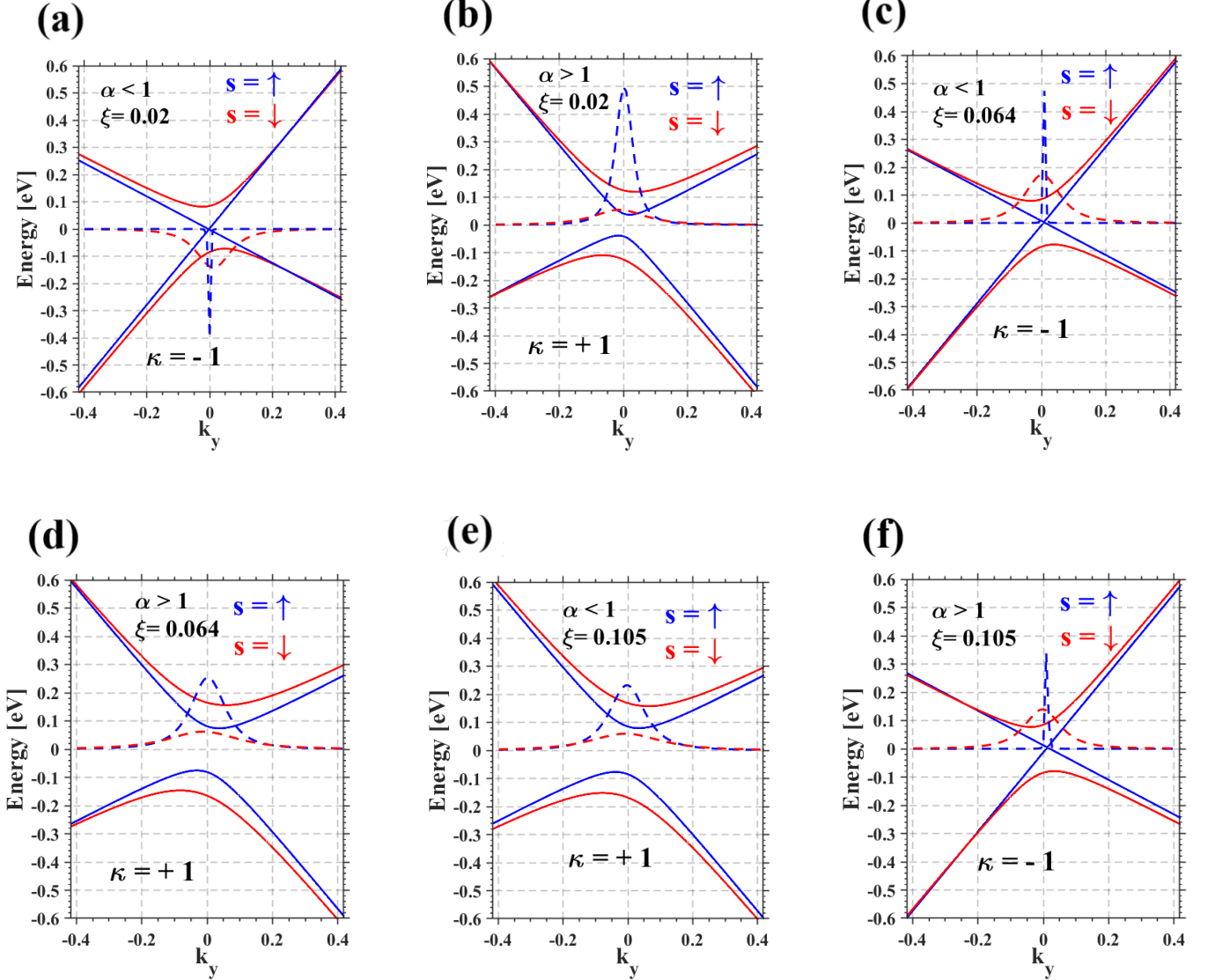


FIG. 2: Floquet-engineered band structures and corresponding Berry curvatures of monolayer 1T'-MoS₂ for different spin and valley indices under various light-matter coupling strengths (ξ) and electric field (α). Panels (a-f) display the quasienergy spectra (solid lines) and Berry curvature distributions (dashed lines) for spin-up (red) and spin-down (blue) states at valleys $\kappa = \pm 1$. Panels (a,b) correspond to $\xi \simeq 0.02$ and (c,d) to $\xi \simeq 0.064$, while (e,f) show results for $\xi \simeq 0.105$.

the light field ($\xi = 0$), the system exhibits the expected structure of a quantum spin Hall insulator, characterized by opposite contributions from the spin-up and spin-down channels. As shown in panel 3 (a), the spin-up Hall response is positive throughout the vicinity of the gap, while panel 3 (b) shows that the spin-down sector contributes with equal magnitude but opposite sign, yielding a nearly vanishing total Hall conductivity as expected from time-reversal symmetry. The plateau-like features emerging around $E_F = 0$ indicate the SOC gap of the 1T' structure.

With the introduction of Floquet driving ($\xi > 0$), substantial modifications appear in the magnitude and structure of the Hall response. For small light-matter coupling

$\xi = 0.02$, both spin-resolved Hall conductivities begin to deviate from their equilibrium values, showing ridge-like dispersive features near the band edges. This reflects the Floquet-induced renormalization of the band gap and the redistribution of Berry curvature around the avoided crossings generated by the light field. The valley-resolved panels (c) and (d) further clarify that the Floquet field breaks the balance between the $\kappa = \pm 1$ valleys, producing a clear valley-contrasting Hall response that does not exist in the equilibrium system. Notably, the $\kappa = +1$ valley (panel (c)) develops a pronounced negative plateau near the Fermi level, whereas the $\kappa = -1$ valley (panel (d)) acquires an enhanced positive response, consistent with Floquet-induced valley polarization.

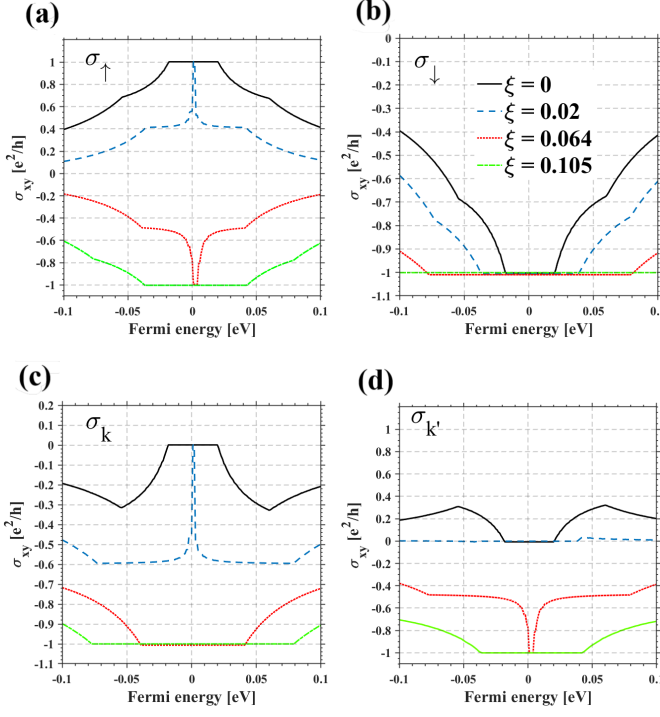


FIG. 3: Spin- and valley-resolved anomalous Hall conductivity σ_{xy} of monolayer $1T'$ -MoS₂ as a function of the Fermi energy for different Floquet coupling strengths $\xi = 0$ (black solid), $\xi = 0.02$ (blue dashed), $\xi = 0.064$ (red dotted), and $\xi = 0.105$ (green solid) for $\alpha < 1$. Panels (a) and (b) correspond to the spin-up and spin-down Hall conductivities, respectively, while panels (c) and (d) show the valley-resolved responses for $\kappa = +1$ and $\kappa = -1$.

As ξ increases to $\xi = 0.064$, the system enters the regime where Floquet hybridization becomes strong enough to compete with the intrinsic inversion-driven SOC. In this intermediate regime, both the spin-up and spin-down channels display nearly quantized Hall plateaus close to $\sigma_{xy} \approx -e^2/h$, signifying the appearance of Floquet-engineered topological gaps with finite Chern number. The valley Hall response becomes strongly symmetric: the $\kappa = \pm 1$ sector develop a deep negative minimum at the Fermi level.

For even stronger drive, $\xi = 0.105$, the Hall conductivity becomes dominated by the Floquet-induced topological bands. The spin-resolved conductivities in panels (a) and (b) clearly show $\sigma_{xy} \sim -e^2/h$. The emergence of such plateaus is consistent with a transition into a P-QHI phase, where the system acquires a non-zero total Chern number due to the breaking of time-reversal symmetry by circular polarization. The valley-resolved panels confirm this transition: the $\kappa = \pm 1$ valley (panel (c) and (d)) develops a broad quantized plateau around $\sigma_{xy} \approx -e^2/h$, demonstrating that the Floquet field induces same sign effective Berry curvature in the two valleys.

Overall, these results demonstrate that Floquet engineering provides an efficient mechanism for controlling the spin and valley Hall responses in $1T'$ -MoS₂. Weak illumination induces renormalization of the intrinsic topo-

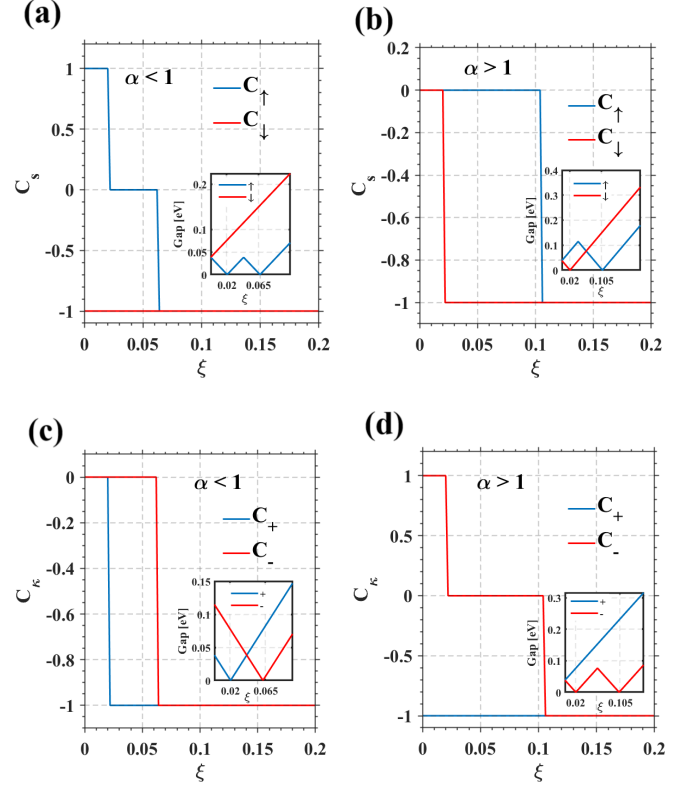


FIG. 4: Spin and valley Chern numbers of monolayer $1T'$ -MoS₂ as a function of the Floquet coupling strength (ξ) for different electric field amounts. Panels (a,b) show the spin Chern numbers C_\uparrow and C_\downarrow , while panels (c,d) present the valley Chern numbers C_+ and C_- for $\alpha < 1$ and $\alpha > 1$, respectively. The insets illustrate the variation of the light-induced band gap with ξ for each spin or valley configuration. s,

logical gap, while stronger driving can generate robust Floquet topological phases with sizable spin, valley, and anomalous Hall conductivities. The distinct plateau structures, the strong valley contrast, and the sign reversals across different ξ values collectively highlight the sensitivity of the Hall response to the interplay between spin-orbit coupling, band inversion, and light-matter interactions. These behaviors are in line with the general picture of Floquet topological phase transitions established in related 2D materials and topological insulators, and they confirm that $1T'$ -MoS₂ is an excellent platform for realizing light-tunable spin-valley Hall physics.

Circularly polarized light acts as a time-periodic perturbation that breaks the time-reversal symmetry of the static system and renormalizes spin-valley-resolved mass gaps with a sign and magnitude that depend on the spin and valley indexes and on the drive amplitude ξ . To leading order in a high-frequency expansion one may write the driven Hamiltonian as an effective static Hamiltonian $H_{eff}(\xi)$ in which each spin and valley acquire an ξ -dependent effective mass $m_{\kappa,s}(\xi)$. A change of the sign of $m_{\kappa,s}(\xi)$ corresponds to a band inversion there and produces the observed quantized change of the spin

and valley Chern numbers. According to the Fig. 4 there are three critical ξ for topological phase transition ($\xi \simeq 0.02, 0.064$ and 0.105). In case of $\alpha < 1$, the critical values are $\xi_{c_1}^{<1} \simeq 0.02$ and $\xi_{c_2}^{<1} \simeq 0.064$. The critical Floquet coupling strengths for $\alpha > 1$ are $\xi_{c_1}^{>1} \simeq 0.02$ and $\xi_{c_2}^{>1} \simeq 0.105$.

Panel 4 (a) shows the spin-resolved Chern numbers C_\uparrow (blue) and C_\downarrow (red) of the 1T'-MoS₂ monolayer as functions of the Floquet coupling strength ξ for $\alpha < 1$. The insets show the corresponding gap versus Floquet coupling strength. Two critical Floquet amplitudes, $\xi_{c_1}^{<1} \simeq 0.02$ and $\xi_{c_2}^{<1} \simeq 0.064$, are clearly visible and mark successive topological phase transitions. For $\xi < \xi_{c_1}^{<1}$ the system is in a compensated spin-opposite topological phase (QSH) characterized by $(C_\uparrow, C_\downarrow) = (+1, -1)$, corresponding to a vanishing total Chern number $C_{\text{tot}} = 0$. At $\xi = \xi_{c_1}^{<1}$ the spin-up gap closes and reopens (or sign of the mass is changed), and C_\uparrow jumps discontinuously from $+1$ to 0 , while C_\downarrow remains fixed at -1 . This produces an intermediate Floquet-induced Chern-insulating phase for $\xi_{c_1}^{<1} < \xi < \xi_{c_2}^{<1}$ with $(C_\uparrow, C_\downarrow) = (0, -1)$ and a nonzero total Chern number $C_{\text{tot}} = -1$.

At the second critical amplitude $\xi_{c_2}^{<1} = 0.064$, the spin-up sector undergoes another gap closing-reopening, again accompanied by a discrete change in its Chern number. The spin-down channel remains topologically inert throughout and retains $C_\downarrow = -1$. The inset highlights the closing of the spin-up gap at both $\xi_{c_1}^{<1}$ and $\xi_{c_2}^{<1}$, confirming that each topological transition is mediated by a bulk gap closure. These results reveal a rich multi-step, spin-selective Floquet control of topology in 1T'-MoS₂, enabling a sequence of distinct topological phases with corresponding changes in the number and chirality of edge states and in the quantized Hall and spin-Hall responses.

Panel 4 (b) is same as (a) but for $\alpha > 1$. For both spin sectors, the Chern number remains trivial, $C_\downarrow = 0$, for $\xi < \xi_{c_1}^{>1}$, where $\xi_{c_1}^{>1} \simeq 0.02$. At this first critical coupling the spin-down gap closes (inset), indicating a Floquet-induced band inversion. After the reopening of the gap, the Chern number jumps to $C_\downarrow = -1$ for $\xi > \xi_{c_1}^{>1}$ and remains constant afterward. There is another gap closing at $\xi = \xi_{c_2}^{>1} \simeq 0.105$ for spin-up component of the Chern number whereas C_\uparrow changes from zero to the -1 . This leads to the topological phase transition from S-QHI to P-QHI as is described in table I, and for $\xi > \xi_{c_2}^{>1}$ both components remains constant as $(C_\uparrow, C_\downarrow) = (-1, -1)$.

These results demonstrate that, for $\alpha > 1$, the Floquet field induces spin-selective and multi-step topological transitions. Both spins undergo a band inversion at $\xi_{c_1}^{>1}$ and $\xi_{c_2}^{>1}$, but for once. The intermediate interval $\xi_{c_1}^{>1} < \xi < \xi_{c_2}^{>1}$ therefore realizes a S-QHI phase, while regions before and after this interval host different topological states.

Panel 4 (c) presents the valley-resolved Chern numbers C_κ of 1T'-MoS₂ as a function of the Floquet coupling strength ξ in the regime $\alpha < 1$. The blue and red curves correspond to the $\kappa = +$ and $\kappa = -$ valleys, respectively.

For small driving amplitudes, both valleys remain topologically trivial with $C_+ = C_- = 0$. As ξ increases, the $\kappa = +$ valley undergoes a topological transition at a critical value $\xi_{c_1}^{<1} \simeq 0.02$, where its Chern number abruptly changes from 0 to -1 . The $\kappa = -$ valley remains trivial until a larger critical coupling $\xi_{c_2}^{<1} \simeq 0.064$, at which point it also undergoes a band inversion and acquires a Chern number $C_- = -1$. These two distinct transition points define three topological regimes: a trivial phase at small ξ , an intermediate valley-polarized topological phase in which only the $\kappa = +$ valley contributes a nonzero Chern number, and a P-QHI at larger ξ where both valleys are nontrivial. The inset displays the evolution of the quasienergy gaps at each valley, showing that each change in C_κ is associated with a corresponding gap closing and reopening. This confirms that the Floquet drive induces valley-selective band inversions, with the two valleys responding differently due to the condition $\alpha < 1$. The resulting topological structure has direct implications for measurable properties: the total Hall conductivity $\sigma_{xy} = (C_+ + C_-)e^2/h$ exhibits quantized values of 0 , $-e^2/h$, and $-2e^2/h$ across the three regimes. In particular, the intermediate region hosts a valley-polarized topological state characterized by a single chiral edge mode originating solely from the $\kappa = +$ valley. Nonetheless, the figure clearly demonstrates that Floquet engineering provides a tunable and valley-selective route to inducing topological phases in 1T'-MoS₂, highlighting its potential for optically controlled topological valleytronics.

Panel 4 (d) shows the valley-resolved Chern numbers C_κ of 1T'-MoS₂ as a function of the Floquet coupling strength ξ for the case $\alpha > 1$, together with the corresponding quasienergy gaps shown in the inset. In this regime, the two valleys exhibit markedly different Chern numbers at low driving strengths: the $\kappa = +$ with $C_+ = -1$, while the $\kappa = -$ valley is characterized by $C_- = +1$. As the Floquet coupling increases, the $\kappa = -$ valley undergoes a topological phase transition at a critical value $\xi_{c_1}^{>1} \simeq 0.02$, where its Chern number switches abruptly from $+1$ to 0 as the gap closes and reopens, as clearly reflected in the inset. In contrast, the gap of the $\kappa = +$ valley increases monotonically without closing over the same range of ξ , which explains why its Chern number remains unchanged throughout the initial evolution. For interval $\xi_{c_1}^{>1} < \xi < \xi_{c_2}^{>1}$ there is an intermediate phase characterized by $C_- = 0$ and $C_+ = -1$. Once the second transition at $\xi_{c_2}^{>1}$ occurs, both valleys adopt the same Chern number $C_\kappa = -1$, implying that the system enters a P-QHI phase. The inset further highlights the valley-selective gap closing responsible for this asymmetry, with the $\kappa = -$ valley uniquely sensitive to the Floquet-induced inversion when $\alpha > 1$. From a physical perspective, this behavior reveals that the parameter α governs the relative susceptibility of the valleys to drive-induced mass renormalization, leading to a scenario in which only the $\kappa = -$ valley undergoes a topological inversion before both valleys eventually synchronize in the

final $C_\kappa = -1$ phase. The resulting total Chern number changes from $C_{\text{tot}} = 0$ at small ξ to $C_{\text{tot}} = -2$ after the transition, indicating a switch from a BI initial state to a fully topological phase with two co-propagating chiral edge channels. Overall, the figure demonstrates that for $\alpha > 1$ the Floquet drive produces a single-valley-driven topological transition that leads directly into a unified topological phase, illustrating a sharply contrasting behavior relative to the $\alpha < 1$ regime and emphasizing the high degree of valley-specific tunability achievable through Floquet engineering in 1T'-MoS₂.

From our numerical results for $\alpha > 1$, the plateau values of the Chern numbers read:

$$\begin{aligned} \xi < \xi_{c_1}^{>1} : & C_+ = -1, C_- = +1, C_\uparrow = 0, C_\downarrow = 0; \\ \xi_{c_1}^{>1} < \xi < \xi_{c_2}^{>1} : & C_+ = -1, C_- = 0, C_\uparrow = 0, C_\downarrow = -1; \\ \xi > \xi_{c_2}^{>1} : & C_+ = -1, C_- = -1, C_\uparrow = -1, C_\downarrow = -1. \end{aligned}$$

Summing over valleys gives:

$$C_{\text{tot}} = C_+ + C_- = \begin{cases} 0, & \xi < \xi_{c_1}^{>1}, \\ -1, & \xi_{c_1}^{>1} < \xi < \xi_{c_2}^{>1}, \\ -2, & \xi > \xi_{c_2}^{>1}, \end{cases}$$

and summing over spins yields the same result:

$$C_{\text{tot}} = C_\uparrow + C_\downarrow = \begin{cases} 0, & \xi < \xi_{c_1}^{>1}, \\ -1, & \xi_{c_1}^{>1} < \xi < \xi_{c_2}^{>1}, \\ -2, & \xi > \xi_{c_2}^{>1}. \end{cases}$$

Both decompositions thus produce a consistent total Chern number $C_{\text{tot}}(\xi) = 0 \rightarrow -1 \rightarrow -2$, demonstrating internal consistency of the Floquet topological transitions. However, it would be incorrect to write $C_{\text{tot}} = C_{\text{valley}} + C_{\text{spin}}$, since that would double-count the same occupied subspace.

TABLE I: Spin- and valley-resolved Chern numbers versus Floquet driving strength for $\alpha = 1.5$.

Floquet range	C_\uparrow	C_\downarrow	C_+	C_-	C_{tot}	ΔC_{spin}	ΔC_{valley}	Phase
$\xi < 0.02$	0	0	-1	+1	0	0	-1	BI
$0.02 < \xi < 0.105$	0	-1	-1	0	-1	+1/2	-1/2	S-QHI
$\xi > 0.105$	-1	-1	-1	-1	-2	0	0	P-QHI

TABLE II: Spin- and valley-resolved Chern numbers versus Floquet driving strength for $\alpha = 0.5$.

Floquet range	C_\uparrow	C_\downarrow	C_+	C_-	C_{tot}	ΔC_{spin}	ΔC_{valley}	Phase
$\xi < 0.02$	+1	-1	0	0	0	+1	0	QSH
$0.02 < \xi < 0.064$	0	-1	-1	0	-1	+1/2	-1/2	S-QHI
$\xi > 0.062$	-1	-1	-1	-1	-2	0	0	P-QHI

IV. CONCLUSIONS

The results of this work delineate how circular driving restructures the spin-valley landscape of 1T'-MoS₂ and organizes its nonequilibrium topological phases. The Floquet-renormalized spectrum exhibits a sequence of drive-controlled gap closings, each accompanied by a redistribution of Berry curvature among the spin and valley sectors. These critical points define boundaries separating quantum spin Hall, valley-polarized, spin-polarized, and Chern insulating regimes. The spin- and valley-resolved Hall conductivities reveal that the response of individual sectors can be tuned independently through the Floquet coupling strength and the electric-field. This tunability originates from distinct light-induced mass renormalizations acting differently on the two valleys and spin channels. Overall, the results identify 1T'-MoS₂ as a material whose topological transport properties can be reconfigured continuously and reversibly by high-frequency driving, highlighting its potential for light-programmable topological functionalities.

V. APPENDIX

Substitute (47) into the Chern integral:

$$C_{\kappa s} = \frac{1}{2\pi} \frac{\hbar^2 \nu_1}{2} (BM_x - AM_z) \int d^2 k \frac{1}{|d|^3}. \quad (53)$$

Introduce the linear variables

$$u \equiv \hbar \nu_1 k_x, \quad v \equiv \hbar k_y.$$

Then

$$d^2 k = dk_x dk_y = \frac{du dv}{\hbar^2 \nu_1},$$

and the denominator becomes

$$D(u, v) = (M_x - Av)^2 + u^2 + (M_z - Bv)^2.$$

Thus

$$C_{\kappa s} = \frac{1}{2\pi} \frac{\hbar^2 \nu_1}{2} (BM_x - AM_z) \int \frac{du dv}{\hbar^2 \nu_1} \frac{1}{[D(u, v)]^{3/2}}. \quad (54)$$

Cancel the $\hbar^2 \nu_1$ prefactors:

$$C_{\kappa s} = \frac{1}{4\pi} (BM_x - AM_z) \int du dv \frac{1}{[D(u, v)]^{3/2}}. \quad (55)$$

Write the quadratic form in v :

$$D(u, v) = u^2 + (A^2 + B^2) v^2 - 2v(AM_x + BM_z) + M_x^2 + M_z^2.$$

Complete the square by defining

$$\tilde{w} \equiv \sqrt{A^2 + B^2} v - \frac{AM_x + BM_z}{\sqrt{A^2 + B^2}}.$$

Then

$$D(u, v) = u^2 + \tilde{w}^2 + M_x^2 + M_z^2 - \frac{(AM_x + BM_z)^2}{A^2 + B^2}.$$

Define the effective mass

$$M_{\text{eff}}^2 \equiv M_x^2 + M_z^2 - \frac{(AM_x + BM_z)^2}{A^2 + B^2}.$$

A short algebraic rearrangement shows

$$M_{\text{eff}}^2 = \frac{(BM_x - AM_z)^2}{A^2 + B^2}.$$

(Indeed this identity is the numerator/denominator algebra behind the simplification of the integral.)

The Jacobian for $(u, v) \mapsto (u, \tilde{w})$ is $|\partial(u, v)/\partial(u, \tilde{w})| = 1/\sqrt{A^2 + B^2}$ since $\tilde{w} = \sqrt{A^2 + B^2}v - \text{const.}$ Therefore

$$\int du dv \frac{1}{[D(u, v)]^{3/2}} = \frac{1}{\sqrt{A^2 + B^2}} \int du d\tilde{w} \frac{1}{[u^2 + \tilde{w}^2 + M_{\text{eff}}^2]^{3/2}}. \quad (56)$$

Let $r^2 = u^2 + \tilde{w}^2$, $du d\tilde{w} = r dr d\theta$. The angular integral gives a factor 2π :

$$\int du d\tilde{w} \frac{1}{(r^2 + M_{\text{eff}}^2)^{3/2}} = 2\pi \int_0^\infty \frac{r dr}{(r^2 + M_{\text{eff}}^2)^{3/2}}.$$

Evaluate the radial integral (standard):

$$\int_0^\infty \frac{r dr}{(r^2 + a^2)^{3/2}} = \frac{1}{a}.$$

Hence

$$\int du dv \frac{1}{[D(u, v)]^{3/2}} = \frac{1}{\sqrt{A^2 + B^2}} 2\pi \frac{1}{M_{\text{eff}}}.$$

Using $M_{\text{eff}} = \frac{|BM_x - AM_z|}{\sqrt{A^2 + B^2}}$ we obtain the closed form

$$\int du dv \frac{1}{[D(u, v)]^{3/2}} = 2\pi \frac{1}{|BM_x - AM_z|}.$$

Substitute back into the expression for $C_{\kappa s}$:

$$\begin{aligned} C_{\kappa s} &= \frac{1}{4\pi} (BM_x - AM_z) \left[2\pi \frac{1}{|BM_x - AM_z|} \right] \\ &= \frac{1}{2} \text{sgn}(BM_x - AM_z). \end{aligned} \quad (57)$$

Recalling $A = s\nu_2$ and $B = \kappa\nu_+$, this is

$$C_{\kappa s} = \frac{1}{2} \text{sgn}(\kappa\nu_+ M_x - s\nu_2 M_z). \quad (58)$$

CONFLICT OF INTERESTS

The authors have no conflicts to disclose.

* mortezaie.mm71@gmail.com

- [1] C. L. Kane and E. J. Mele, Quantum spin hall effect in graphene, *Phys. Rev. Lett.* **95**, 226801 (2005).
- [2] M.-C. Chang and M.-F. Yang, Optical signature of topological insulators, *Physical Review B—Condensed Matter and Materials Physics* **80**, 113304 (2009).
- [3] M. König, S. Wiedmann, C. Brüne, A. Roth, H. Buhmann, L. W. Molenkamp, X.-L. Qi, and S.-C. Zhang, Quantum spin hall insulator state in hgte quantum wells, *Science* **318**, 766 (2007), <https://www.science.org/doi/pdf/10.1126/science.1148047>.
- [4] M. König, H. Buhmann, L. W. Molenkamp, T. Hughes, C.-X. Liu, X.-L. Qi, and S.-C. Zhang, The quantum spin hall effect: Theory and experiment, *Journal of the Physical Society of Japan* **77**, 031007 (2008), <https://doi.org/10.1143/JPSJ.77.031007>.
- [5] D. N. Sheng, Z. Y. Weng, L. Sheng, and F. D. M. Haldane, Quantum spin-hall effect and topologically invariant chern numbers, *Phys. Rev. Lett.* **97**, 036808 (2006).
- [6] M. Z. Hasan and C. L. Kane, Colloquium: Topological insulators, *Rev. Mod. Phys.* **82**, 3045 (2010).
- [7] X.-L. Qi and S.-C. Zhang, Topological insulators and superconductors, *Rev. Mod. Phys.* **83**, 1057 (2011).
- [8] B. A. Bernevig, T. L. Hughes, and S.-C. Zhang, Quantum spin hall effect and topological phase transition in hgte quantum wells, *Science* **314**, 1757 (2006), <https://www.science.org/doi/pdf/10.1126/science.1133734>.
- [9] M. König, S. Wiedmann, C. Brüne, A. Roth, H. Buhmann, L. W. Molenkamp, X.-L. Qi, and S.-C. Zhang, Quantum spin hall insulator state in hgte quantum wells, *Science* **318**, 766 (2007).
- [10] C. Liu, T. L. Hughes, X.-L. Qi, K. Wang, and S.-C. Zhang, Quantum spin hall effect in inverted type-ii semiconductors, *Phys. Rev. Lett.* **100**, 236601 (2008).
- [11] Y. Ando, Topological insulator materials, *Journal of the Physical Society of Japan* **82**, 102001 (2013), <https://doi.org/10.7566/JPSJ.82.102001>.
- [12] I. Knez, R.-R. Du, and G. Sullivan, Evidence for helical edge modes in inverted InAs/GaSb quantum wells, *Phys. Rev. Lett.* **107**, 136603 (2011).
- [13] L. Du, I. Knez, G. Sullivan, and R.-R. Du, Robust helical edge transport in gated InAs/GaSb bilayers, *Phys. Rev. Lett.* **114**, 096802 (2015).
- [14] C.-C. Liu, W. Feng, and Y. Yao, Quantum spin hall effect in silicene and two-dimensional germanium, *Phys. Rev. Lett.* **107**, 076802 (2011).
- [15] M. Ezawa, A topological insulator and helical zero mode in silicene under an inhomogeneous electric field, *New Journal of Physics* **14**, 033003 (2012).

- [16] S. Murakami, Quantum spin hall effect and enhanced magnetic response by spin-orbit coupling, *Phys. Rev. Lett.* **97**, 236805 (2006).
- [17] F. Reis, G. Li, L. Dudy, M. Bauernfeind, S. Glass, W. Hanke, R. Thomale, J. Schäfer, and R. Claessen, Bismuthene on a sic substrate: A candidate for a high-temperature quantum spin hall material, *Science* **357**, 287 (2017), <https://www.science.org/doi/pdf/10.1126/science.aai8142>.
- [18] Y. Xu, B. Yan, H.-J. Zhang, J. Wang, G. Xu, P. Tang, W. Duan, and S.-C. Zhang, Large-gap quantum spin hall insulators in tin films, *Phys. Rev. Lett.* **111**, 136804 (2013).
- [19] X. Qian, J. Liu, L. Fu, and J. Li, Quantum spin hall effect in two-dimensional transition metal dichalcogenides, *Science* **346**, 1344 (2014).
- [20] S. Tang, C. Zhang, D. Wong, Z. Pedramrazi, H.-Z. Tsai, C. Jia, B. Moritz, M. Claassen, H. Ryu, S. Kahn, J. Jiang, H. Yan, M. Hashimoto, D. Lu, R. G. Moore, C.-C. Hwang, C. Hwang, Z. Hussain, Y. Chen, M. M. Ugeda, Z. Liu, X. Xie, T. P. Devereaux, M. F. Crommie, S.-K. Mo, and Z.-X. Shen, Quantum spin hall state in monolayer $1t'$ -wte₂, *Nature Physics* **13**, 683 (2017).
- [21] Z. Fei, T. Palomaki, S. Wu, W. Zhao, X. Cai, B. Sun, P. Nguyen, J. Finney, X. Xu, and D. H. Cobden, Edge conduction in monolayer wte₂, *Nature Physics* **13**, 677 (2017).
- [22] L. Fu and C. L. Kane, Topological insulators with inversion symmetry, *Phys. Rev. B* **76**, 045302 (2007).
- [23] R. Yu, W. Zhang, H.-J. Zhang, S.-C. Zhang, X. Dai, and Z. Fang, Quantized anomalous hall effect in magnetic topological insulators, *Science* **329**, 61 (2010), <https://www.science.org/doi/pdf/10.1126/science.1187485>.
- [24] J. Wang, B. Lian, and S.-C. Zhang, Quantum anomalous hall effect in magnetic topological insulators, *Physica Scripta* **2015**, 014003 (2015).
- [25] S. Rachel, Interacting topological insulators: a review, *Reports on Progress in Physics* **81**, 116501 (2018).
- [26] C.-C. Liu, H. Jiang, and Y. Yao, Low-energy effective hamiltonian involving spin-orbit coupling in silicene and two-dimensional germanium and tin, *Phys. Rev. B* **84**, 195430 (2011).
- [27] H.-Z. Lu, A. Zhao, and S.-Q. Shen, Quantum transport in magnetic topological insulator thin films, *Phys. Rev. Lett.* **111**, 146802 (2013).
- [28] T. Oka and H. Aoki, Photovoltaic hall effect in graphene, *Phys. Rev. B* **79**, 081406 (2009).
- [29] Y. H. Wang, H. Steinberg, P. Jarillo-Herrero, and N. Gedik, Observation of floquet-bloch states on the surface of a topological insulator, *Science* **342**, 453 (2013), <https://www.science.org/doi/pdf/10.1126/science.1239834>.
- [30] M. Chhowalla, H. S. Shin, G. Eda, L.-J. Li, K. P. Loh, and H. Zhang, The chemistry of two-dimensional layered transition metal dichalcogenide nanosheets, *Nature Chemistry* **5**, 263 (2013).
- [31] Q. H. Wang, K. Kalantar-Zadeh, A. Kis, J. N. Coleman, and M. S. Strano, Electronics and optoelectronics of two-dimensional transition metal dichalcogenides, *Nature Nanotechnology* **7**, 699 (2012).
- [32] S. Manzeli, D. Ovchinnikov, D. Pasquier, O. V. Yazyev, and A. Kis, 2d transition metal dichalcogenides, *Nature Reviews Materials* **2**, 17033 (2017).
- [33] K. F. Mak, C. Lee, J. Hone, J. Shan, and T. F. Heinz, Atomically thin mos₂: A new direct-gap semiconductor, *Phys. Rev. Lett.* **105**, 136805 (2010).
- [34] D. Xiao, G.-B. Liu, W. Feng, X. Xu, and W. Yao, Coupled spin and valley physics in monolayers of mos₂ and other group-vi dichalcogenides, *Phys. Rev. Lett.* **108**, 196802 (2012).
- [35] J. Heising and M. G. Kanatzidis, Exfoliated and restacked mos₂ and ws₂: ionic or neutral species? encapsulation and ordering of hard electropositive cations, *Journal of the American Chemical Society* **121**, 11720 (1999).
- [36] A.-Y. Lu, H. Zhu, J. Xiao, C.-P. Chuu, Y. Han, M.-H. Chiu, C.-C. Cheng, C.-W. Yang, K.-H. Wei, Y. Yang, *et al.*, Janus monolayers of transition metal dichalcogenides, *Nature nanotechnology* **12**, 744 (2017).
- [37] S. Wu, V. Fatemi, Q. D. Gibson, K. Watanabe, T. Taniguchi, R. J. Cava, and P. Jarillo-Herrero, Observation of the quantum spin hall effect up to 100 kelvin in a monolayer crystal, *Science* **359**, 76 (2018), <https://www.science.org/doi/pdf/10.1126/science.aan6003>.
- [38] J. Chen, L. Wang, M. Zhang, L. Zhou, R. Zhang, L. Jin, X. Wang, H. Qin, Y. Qiu, J. Mei, F. Ye, B. Xi, H. He, B. Li, and G. Wang, Evidence for magnetic skyrmions at the interface of ferromagnet/topological-insulator heterostructures, *Nano Letters* **19**, 6144 (2019).
- [39] N. Katsuragawa, M. Nishizawa, T. Nakamura, T. Inoue, S. Pakdel, S. Maruyama, S. Katsumoto, J. J. Palacios, and J. Haruyama, Room-temperature quantum spin hall phase in laser-patterned few-layer 1t- mos₂, *Communications Materials* **1**, 51 (2020).
- [40] L. Xu, Y. Li, Y. Fang, H. Zheng, W. Shi, C. Chen, D. Pei, D. Lu, M. Hashimoto, M. Wang, L. Yang, X. Feng, H. Zhang, F. Huang, Q. Xue, K. He, Z. Liu, and Y. Chen, Topology hierarchy of transition metal dichalcogenides built from quantum spin hall layers, *Advanced Materials* **35**, 2300227 (2023).
- [41] T. Kitagawa, T. Oka, A. Brataas, L. Fu, and E. Demler, Transport properties of nonequilibrium systems under the application of light: Photoinduced quantum hall insulators without landau levels, *Phys. Rev. B* **84**, 235108 (2011).
- [42] T. Mikami, S. Kitamura, K. Yasuda, N. Tsuji, T. Oka, and H. Aoki, Brillouin-wigner theory for high-frequency expansion in periodically driven systems: Application to floquet topological insulators, *Physical Review B* **93**, 144307 (2016).
- [43] H. Dehghani, T. Oka, and A. Mitra, Dissipative floquet topological systems, *Phys. Rev. B* **90**, 195429 (2014).
- [44] M. Claassen, C. Jia, B. Moritz, and T. P. Devereaux, All-optical materials design of chiral edge modes in transition-metal dichalcogenides, *Nature Communications* **7**, 13074 (2016).
- [45] H. Hübener, M. A. Sentef, U. De Giovannini, A. F. Kemper, and A. Rubio, Creating stable floquet-weyl semimetals by laser-driving of 3d dirac materials, *Nature Communications* **8**, 13940 (2017).
- [46] P. M. Perez-Piskunow, G. Usaj, C. A. Balseiro, and L. E. F. F. Torres, Floquet chiral edge states in graphene, *Phys. Rev. B* **89**, 121401 (2014).
- [47] L. E. F. Foa Torres, P. M. Perez-Piskunow, C. A. Balseiro, and G. Usaj, Multiterminal conductance of a floquet topological insulator, *Phys. Rev. Lett.* **113**, 266801 (2014).
- [48] G. Usaj, P. M. Perez-Piskunow, L. E. F. Foa Torres, and C. A. Balseiro, Irradiated graphene as a tunable floquet

- topological insulator, Phys. Rev. B **90**, 115423 (2014).
- [49] B. Das, D. Sen, and S. Mahapatra, Tuneable quantum spin hall states in confined $1t'$ transition metal dichalcogenides, Scientific Reports **10**, 6670 (2020).
- [50] D. Wang, A. Hu, J.-P. Lv, and G. Jin, Electric field modulated valley- and spin-dependent electron retroreflection and klein tunneling in a tilted $n-p-n$ junction of monolayer $1T'-\text{mos}_2$, Phys. Rev. B **107**, 035301 (2023).